Design, Fabrication and Testing of Microacoustic Metagratings at Ultra-High Frequencies

Anton Melnikov[1a], Sören Köble[1b], Severin Schweiger[1], Yan Kei Chiang[2], Steffen Marburg[3], and David A. Powell[2]

[1] *Fraunhofer Institute for Photonic Microsystems, Dresden, Germany*

[a] *Email: anton.melnikov@tum.de*

[b] *Email: soeren.koeble@ipms.fraunhofer.de*

[2] *School of Engineering and Information Technology, University of New South Wales, Canberra, Australia*

[3] *Chair of Vibro-Acoustics of Vehicles and Machines, Technical University of Munich, Germany*

Abstract

The recently proposed bianisotropic acoustic metagratings offer promising opportunities for passive acoustic wavefront manipulation, which is of particular interest for flat acoustic lenses and ultra-high frequency ultrasound imaging. In this work we scale up the concept of acoustic metagratings to MHz frequencies for airborne ultrasound and thus to a microscopic size of metagrating geometry. This leads to strongly increasing thermoviscous effects, which cause a drop in efficiency and a frequency reduction of the transmission peak. We present several microacoustic metagrating designs optimized for refraction of a normally incident wave towards $-35°$ at 2 MHz, with and without including the thermoviscous effects in the modeling approach. Furthermore, we fabricate and experimentally investigate the designs, demonstrating the feasibility of microacoustic metagratings for anomalous refraction at ultra-high frequencies. This article is a summary of Ref. [1].

Introduction

Acoustic metamaterials enable the creation of unique material properties that do not exist in nature [2, 3, 4, 5], such as negative bulk modulus and negative dynamic mass density [6, 7]. These properties have drawn interest in unconventional acoustic wave manipulation, leading to a wide range of applications, including acoustic cloaking [8], subwavelength acoustic barriers [9, 10], flat acoustic lenses [11], and ultrasonic imaging with subwavelength resolution. Gradient metasurfaces, including reflecting and refracting designs, have been experimentally proven to be an effective passive approach for wavefront control in ultrasonic imaging and acoustic lenses, such as acoustic Fresnel lenses. In the case of airborne ultrasound, ultra-high frequency ultrasound, which starts from 0.5 MHz, poses challenges due to thermoviscous losses at sound-hard boundaries [12, 13]. The use of thin acoustic channels and Helmholtz resonators in gradient acoustic metasurfaces exacerbates this problem, leading to a need for alternative solutions. Bianisotropic metagratings [14, 15, 16] (see Fig. 1) show promise in this ultra-high frequency range, as their geometrical features are larger than those of gradient metasurfaces. However, scaling to ultra-high frequency ultrasound has never been investigated due to the challenges in manufacturing such microscopic structures and the need to make the design insensitive to thermoviscous losses. Recent developments in the additive manufacturing of microscopic structures, particularly two-photon lithography, have overcome one of the major hurdles in the experimental realization of microacoustic metagratings.

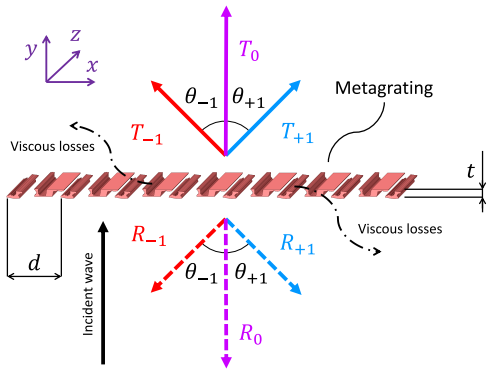

Figure 1: Microacoustic metagrating with three diffraction orders and viscous losses with a normal incident wave. Refracted and reflected wavefronts are indicated by solid and dashed arrows, respectively. The diffraction order is indicated by the subscripts. The global metagrating parameters are the lattice constant d and the grating thickness t. Adopted from Ref. [1]

We present a novel concept of microacoustic metagratings in airborne ultra-high frequency ultrasound, which can be used for flat acoustics, ultrasound imaging, and acoustic spectroscopy with high spatial and temporal resolution. We set the target frequency to 2 MHz, which is beyond the previously discussed frequency range in literature (see Ref.[1]). We chose a range of λ and d values that support only three propagating diffraction orders for both refracted and reflected waves (-1, 0, and +1). The metagrating lattice constant of 299 μm is determined by the Bragg's condition, where the -1st diffraction order is aligned with the desired angle of -35.0 degrees. The resulting metagrating can redirect the wave in six different directions (three transmitted and three reflected diffraction orders) with the possibility of absorption as an additional energy channel. We use the finite element method (FEM) framework to apply different design strategies, including thermoviscous effects, to maximize the energy transmitted into the -1st diffraction order. We design and manufacture three different microacoustic metagratings

using two-photon polymerization, which has not been explored for acoustic metamaterials before. Our advanced designs achieve highly directional refraction due to the optimized meta-atoms' bianisotropic properties [17, 18] and the improvement of the models compared to commonly used lossless approaches, despite some energy dissipation due to viscous losses in the narrow slits. These metagratings can be used for various ultrasound applications, such as flat acoustic lenses for ultrasound imaging with high temporal and spatial resolution or directional shaping of high-frequency ultrasonic transducers for gesture recognition.

Methods

Design. The COMSOL Multiphysics software with Acoustics Module was used to solve the linearized Navier-Stokes equations for numerical analysis. The model assumed an infinite metagrating in a two-dimensional space, with only one strip of length d being modeled. To ensure solution periodicity, a Bloch-Floquet boundary condition was imposed. Perfectly matched layers (PML) were utilized to model the infinite domain extension above and below the metagrating. The transmission and the reflection coefficients then follow as

$$T_n = \frac{a_n^T}{a_{\text{inc}}} \qquad R_n = \frac{a_n^R}{a_{\text{inc}}} \tag{1}$$

and the absorption coefficient as

$$\alpha = 1 - \sum_n |T_n|^2 - \sum_n |R_n|^2,\ n \in \{0, \pm 1\}. \tag{2}$$

The transmitted energy distribution follows as

$$\tau_n = \frac{|T_n|^2}{|T_{-1}|^2 + |T_0|^2 + |T_{+1}|^2}. \tag{3}$$

To enhance the performance of an existing meta-atom geometry, shape optimization (COMSOL Optimization Module) was employed. The free fhape boundary method was utilized to optimize the designs B and C. The boundary of the geometry to be deformed was moved while the Finite Element Method (FEM) mesh was deformed around the geometry based on the smoothing type. To achieve this, the three-term Yeoh hyperelastic model was used with a stiffening factor of 10, which is an extension of the neo-Hookean material. The final geometries of designs B and C were attained after 26 and 101 iterations, respectively. Design C's initial state was created by performing topology optimization using the density model in conjunction with the Helmholtz equation. In this instance, the mesh stayed unchanged, and a domain control variable was varied as it was discretized on the mesh. The filter type was set to Helmholtz, the projection type to hyperbolic tangent, the interpolation type to linear, and the element order to linear. Design C's intermediate geometry was achieved after 48 iterations.

Fabrication. Samples were produced using a two-photon polymerization based additive manufacturing method. The Photonic Professional GT2 (Nanoscribe GmbH, Germany) was utilized for the process and has a build volume of $10 \times 10 \times 0.8\,\text{cm}^3$. The voxel shape has an elliptic shape, and its size ranges from $0.1\,\mu$m to $5\,\mu$m in radius (r_v) and from $0.3\,\mu$m to $15\,\mu$m in height (z_v), which depends on the optical properties of the photoresist and the illumination process parameters. The fabrication process involved scanning the voxel through the photoresist based on CAD models. After curing, the excess photoresist was removed, and the resulting structures were detached from the substrate after drying. For focusing, a 10× numerical aperture (NA) 0.3 immersion objective was used for the grating holder, and a 25× NA 0.8 immersion objective was used for the grating sample. The photoresists IP-Q and IP-S, obtained from Nanoscribe GmbH, Germany, were utilized for the process.

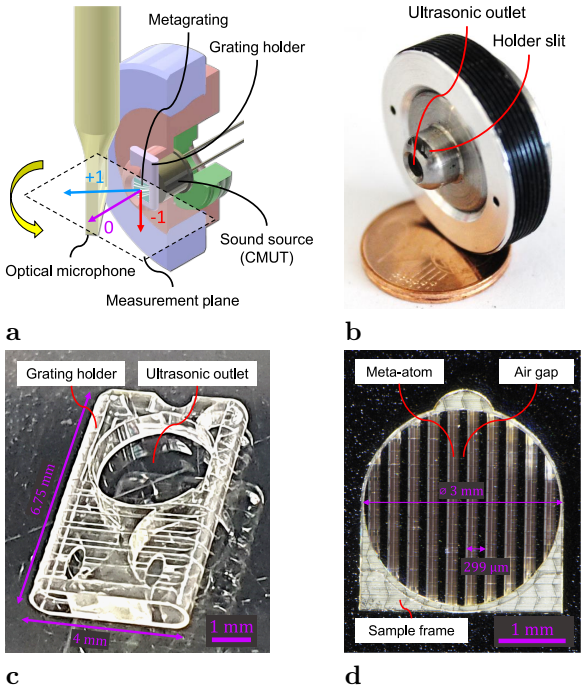

Figure 2: Experimental setup. **a** The rotatable holder including transducer and the moving laser microphone. **b** Photograph of the rotatable holder. **c** Micrograph of the grating holder created by two-photon lithography. **d** Micrograph of the microacoustic metagrating sample. Adopted from Ref. [1]

Testing The experimental setup depicted in Fig. 2 comprises a configuration connecting a microacoustic metagrating with a sound source, which is positioned on a system that allows the assembly to move relative to a microphone. The sound source employed is a capacitive micro-machined ultrasound transducer, designed and fabricated in-house and installed on a TO-18 chassis (a transistor-style metal housing) that is clamped into the frame using a screw. For measuring ultra-high frequency ultrasound, we use the Eta450 Ultra optical microphone (Xarion, Austria), which has a frequency range of 50 MHz to 2 MHz. The frequency range is extended up to 2.2 MHz in this work, as only relative sound pressure values are utilized. Motorized stages (Physical Instruments, Ger-

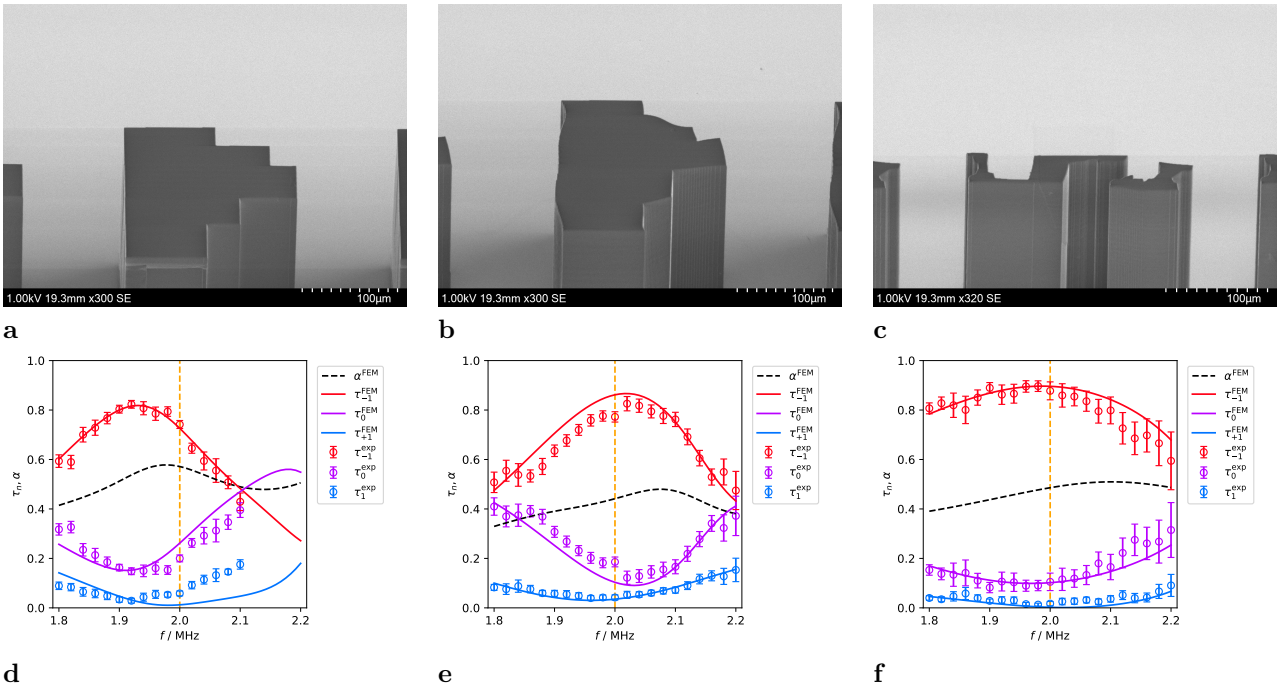

Figure 3: Fabricated microacoutic metagratings and experimental results. ad Design A, semi-analytically optimized lossless metagrating. **be** Design B, reoptimized metagrating including thermoviscous effects. **cf** Design C, broadband and subwavelength microacoustic metagrating. **a-c** SEM micrograph of the meta-atom manufactured by two-photon lithography. **d-f** Experimentally and numerically determined normalized transmission τ_n and numerically determined absorption α. Adopted from Ref. [1]

many) are employed to conduct radial scans in one plane. The directional characteristic of the microphone is disregarded, as it is always aligned with the same side to the axis of rotation on the metagrating. The measured angle lies within $-70° < \theta < 70°$ to avoid collisions between the rotatable holder and the microphone attachment. To hasten the measurement process, the radial axis is constantly moved, triggering sound pressure measurements at a resolution of 0.1°. Continuous stimulation is used for the measurements, with a sinusoidal signal of 10 Vpp and a DC bias of 20 V. The metagrating is aligned with the rotation axis, which is orthogonal to the measurement plane, while the center of the microphone is situated at half the height of the metagrating. The refracted wave is then measured using the optical microphone on a circular trajectory at a radius of 10.66 mm (design A), 8.22 mm (design B), and 8.19 mm (design C) from the metagrating surface.

Results

Design A. Design A is the first metagrating based on the Helmholtz equation, assuming an infinite number of meta-atoms in a 2D model without air viscosity. Lossless structures are optimized with simple shapes and a semianalytical model based on superposition of waveguide modes. The final meta-atom design consists of five rectangles with a thickness of $t = 196\,\mu$m (see Fig. 3a), achieving $|T_{-1}|^2 \approx 0.95$ at 2 MHz in the absence of losses. However, using the more accurate Navier-Stokes equations with air viscosity, transmission towards −1st diffraction order decreases, and the peak shifts to 1.90 MHz with $|T_{-1}|^2 = 0.36$. In Figure 3d, we present the measured and numerically calculated normalized transmission (see Eq. (3)), while the numerical results of the unnormalized transmission are available in Ref. [1]. The simulation results with thermoviscous effects match the experimental results accurately. The maximum τ_{-1} peak determined numerically is at a frequency of 1.93 MHz with $\tau_{-1} = 0.82$, while in the experiment, the peak occurs at 1.92 MHz with $\tau_{-1} = 0.82 \pm 0.02$. Moreover, the experiment also shows the crossing point of τ_{-1} and τ_0 around 2.10 MHz, as predicted by the numerical simulations.

Design B. To improve the efficiency and peak frequency of the acoustic metagrating, a shape reoptimization using FEM with thermoviscous losses was performed. The optimization goal was to maximize the transmission towards the −1st diffraction order, resulting in a maximum transmission of $|T_{-1}|^2 = 0.45$. The final geometry, design B, was fabricated using two-photon polymerization, see Fig. 3b. Comparison between numerical and experimental results for the normalized transmission (see Fig. 3e) shows good agreement, with both indicating a peak at 2.02 MHz and τ_{-1} values of 0.87 and 0.83 ± 0.03, respectively.

Design C. To create design C, in the first step, we use topology optimization to create a new geometry that maximizes T_{-1} without considering thermoviscous losses. The optimization domain is an infinite wall with a thickness limit of $t = \lambda/4$. In the second step, we use the newly created geometry as the initial geometry for a shape optimization that considers thermoviscous losses. The final geometry (see Fig. 3c) achieves

$|T_{-1}|^2 = 0.41$ at the target frequency, with a thickness of only $t = 50\,\mu\text{m} \approx 0.29\lambda$. The experimentally and numerically determined transmission is shown in Figure 3f, where we observe a high amount of energy in the -1 diffraction order. The peak τ_{-1} is expected at 1.98 MHz with $\tau_{-1} = 0.90$ from the numerics, while the experiment shows the peak at 1.96 MHz with $\tau_{-1} = 0.90 \pm 0.02$. Furthermore, $\tau_{-1} = 0.88 \pm 0.04$ at the target frequency, which is better than the peak values of previous designs A and B. The broadband range between 1.80 MHz and 2.08 MHz has $\tau_{-1} > 0.80$, which is an improvement over previous results. Despite having thinner channels closer to the Stoke's boundary layer thickness δ_S (see Ref. [1], this new design demonstrates the best experimental performance among the investigated geometries.

Summary

Anomalous refraction at frequencies of at least 2 MHz has been experimentally proven, which is of significant interest for flat acoustics and ultrasonic imaging with high spatial and temporal resolution. However, it has been shown both numerically and experimentally that thermoviscous effects within metagratings cannot be neglected, leading to a drop in efficiency and a downshift in peak frequency when designs are based on the lossless Helmholtz equation. This problem arises due to the close proximity of the viscous and thermal boundary layer thicknesses to the geometric dimensions of the meta-atoms when shrinking to microscopic dimensions required for ultra-high frequencies. Therefore, to optimize metagrating designs and overcome the drop in performance and frequency downshift, thermoviscous effects should be explicitly modelled.

References

[1] Melnikov, A. *et al.* Microacoustic metagratings at ultra-high frequencies fabricated by two-photon lithography. *Advanced Science* **9**, 2200990 (2022). URL https://onlinelibrary.wiley.com/doi/abs/10.1002/advs.202200990. https://onlinelibrary.wiley.com/doi/pdf/10.1002/advs.202200990.

[2] Cummer, S. A., Christensen, J. & Alù, A. Controlling sound with acoustic metamaterials. *Nature Reviews Materials* **1**, 1–13 (2016). URL https://www.nature.com/articles/natrevmats20161.

[3] Haberman, M. R. & Guild, M. D. Acoustic metamaterials. *Physics Today* **69**, 42–48 (2016).

[4] Ma, G. & Sheng, P. Acoustic metamaterials: From local resonances to broad horizons. *Science Advances* **2**, e1501595 (2016). URL https://advances.sciencemag.org/content/2/2/e1501595?ijkey=6cb527cf80477a8231da3da917ac013183d4d5bb&keytype2=tf_ipsecsha.

[5] Jiménez, N., Umnova, O. & Groby, J.-P. (eds.) *Acoustic Waves in Periodic Structures, Metamaterials, and Porous Media: From Fundamentals to Industrial Applications*, vol. 143 of *Springer eBook Collection* (Springer, Cham, 2021).

[6] Fang, N. *et al.* Ultrasonic metamaterials with negative modulus. *Nature Materials* **5**, 452–456 (2006). URL http://dx.doi.org/10.1038/nmat1644.

[7] Koo, S., Cho, C., Jeong, J.-h. & Park, N. Acoustic omni meta-atom for decoupled access to all octants of a wave parameter space. *Nature Communications* **7** (2016). URL http://dx.doi.org/10.1038/ncomms13012.

[8] Zigoneanu, L., Popa, B.-I. & Cummer, S. A. Three-dimensional broadband omnidirectional acoustic ground cloak. *Nature Materials* **13**, 352–355 (2014). URL https://www.nature.com/articles/nmat3901.

[9] Melnikov, A. *et al.* Acoustic metamaterial capsule for reduction of stage machinery noise. *The Journal of the Acoustical Society of America* **147**, 1491 (2020). URL https://asa.scitation.org/doi/full/10.1121/10.0000857.

[10] Krasikova, M. *et al.* Metahouse: Noise-insulating chamber based on periodic structures. *Advanced Materials Technologies* **8**, 2200711 (2023). URL https://onlinelibrary.wiley.com/doi/abs/10.1002/admt.202200711. https://onlinelibrary.wiley.com/doi/pdf/10.1002/admt.202200711.

[11] Jin, Y., Kumar, R., Poncelet, O., Mondain-Monval, O. & Brunet, T. Flat acoustics with soft gradient-index metasurfaces. *Nature Communications* **10**, 143 (2019).

[12] Ward, G. P. *et al.* Boundary-Layer Effects on Acoustic Transmission Through Narrow Slit Cavities. *Physical Review Letters* **115**, 044302 (2015).

[13] Cotterill, P. A., Nigro, D., Abrahams, I. D., Garcia-Neefjes, E. & Parnell, W. J. Thermo-viscous damping of acoustic waves in narrow channels: A comparison of effects in air and water. *The Journal of the Acoustical Society of America* **144**, 3421 (2018).

[14] Torrent, D. Acoustic anomalous reflectors based on diffraction grating engineering. *Physical Review B* **98**, 060101 (2018).

[15] Craig, S. R., Su, X., Norris, A. & Shi, C. Experimental Realization of Acoustic Bianisotropic Gratings. *Physical Review Applied* **11**, 061002 (2019).

[16] Chiang, Y. K. *et al.* Reconfigurable Acoustic Metagrating for High-Efficiency Anomalous Reflection. *Physical Review Applied* **13**, 064067 (2020).

[17] Quan, L., Ra'di, Y., Sounas, D. L. & Alù, A. Maximum Willis Coupling in Acoustic Scatterers. *Physical Review Letters* **120**, 254301 (2018).

[18] Melnikov, A. *et al.* Acoustic meta-atom with experimentally verified maximum Willis coupling. *Nature Communications* **10**, 1–7 (2019). URL https://www.nature.com/articles/s41467-019-10915-5.